International Journal of Applied Electromagnetics and Mechanics 34 (2010) 73–86
DOI 10.3233/JAE-2010-1088
IOS Press

Time domain microwave imaging for a buried dielectric cylinder by dynamic differential evolution

Ching-Lieh Li[a], Wei Chien[b], Chung-Hsin Huang[c] and Chien-Ching Chiu[a,*]
[a]*Electrical Engineering Department, Tamkang University, Tamsui, Taipei County, Taiwan*
[b]*Electronic Engineering Department, De Lin Institute of Technology Tu-Cheng, Taipei, Taiwan*
[c]*Department of Computer and Communication Engineering, Taipei College of Maritime Technology, Danshui Town, Taipei County, Taiwan*

Abstract. This paper presents the studies of time domain inverse scattering for a two dimensional homogeneous dielectric cylinder buried in a half-space which are based on the finite difference time domain (FDTD) method and the dynamic differential evolution (DDE). For the forward scattering, the FDTD method is employed to calculate the scattered E fields, while for the inverse scattering the DDE scheme is utilized to determine the shape, location and the permittivity of the buried cylindrical scatterer with arbitrary cross section. The subgirdding technique is implemented for the FDTD code in order to model the shape of the cylinder more smoothly. In additions, in order to describe an unknown cylinder with arbitrary cross section more effectively during the course of searching, the closed cubic-spline expansion is adopted to represent the scatterer contour instead of the frequently used trigonometric series. Numerical results demonstrate that, even when the initial guess is far away from the exact one, good reconstruction can be obtained. In addition, the effects of Gaussian noise on the reconstruction results are investigated. Numerical results show that even the measured scattered fields are contaminated with Gaussian noise, DDE is able to yield good reconstructed quality.

Keywords: Time domain inverse scattering, FDTD, subgridding, dynamic differential evolution, homogenous dielectric cylinder

1. Introduction

The objective of the inverse problem of the buried scatterer is to determine the electromagnetic properties of the scatterer from the scattering field measured outside. Due to large domain of applications such as non-destructive problem, medical imaging, geophysical prospecting and determination of underground tunnels and pipelines, etc, the inverse scattering problems related to the buried bodies have a particular importance in the scattering theory. This kind of problem is expected to be difficult due to the fact that the information about the buried unknown scatterer obtained by the limited-view measurement is less than the full-view measurement. Although the incompleteness of the measurement data and the multiple scattering of the scatterer bring out the intrinsic non-uniqueness and ill-posedness of these problems that appear consequentially in the inverse scattering problems [1,2], the study can be applied in widespread use.

*Corresponding author. E-mail: chiu@ee.tku.edu.tu.

Most of the inversion techniques are investigated for the microwave imaging by time-harmonic EM wave illumination [3–10]. However, the application of wideband incidence is important for the microwave imaging because the available information content about unknown objects is more than the only single frequency scattering data alone. The main methods to solve the inverse scattering problems in time domain are Born iterative method (BIM) [11,12] and optimization methods [13–15]. The inverse scattering problems are usually treated by the traditional deterministic methods which are founded on a functional minimization via some gradient-type scheme. The major drawback of these kinds of deterministic methods is that the final reconstructed image is highly dependent on the initial trial guess [4]. In general, they tend to get trapped in local minima when the initial trial solution is far from the exact one. Thus, some population-based stochastic methods, such as genetic algorithm (GA) [5,6, 16], differential evolution (DE) [7,8], and particle swarm optimization (PSO) [9,10,17,18], are proposed to search the global extreme of the inverse problems to overcome the drawback of the deterministic methods. In the 2006, the dynamic differential evolution (DDE) was first proposed to deal with the shape reconstruction of conducting cylinders [19]. Moreover, it was shown that DDE outperforms traditional DE in terms of convergence speed. To the best of our knowledge, there is still no investigation on using the DDE to reconstruct the electromagnetic imaging of homogeneous dielectric cylinders with arbitrary cross section in a half space under time domain.

This paper presents a time domain computational scheme for the microwave imaging of a 2D homogeneous dielectric cylinder with arbitrary shape buried in the subsurface. The forward problem is solved by the FDTD method, for which the subgridding technique [20] is implemented to closely describe the fine structure of the cylinder. The inverse problem is formulated into an optimization one, and then the global searching scheme DDE is used to search the parameter space. Cubic spline interpolation technique [21] is employed to reduce the number of parameters needed to closely describe a cylinder of arbitrary shape as compared to the Fourier series expansion. In Section II, the theoretical formulation for the electromagnetic imaging is presented. The general principle of the DDE scheme and the way we applied it to the imaging problem are described. Numerical results for various objects of different shapes are given in Section III. Section IV is the conclusion.

2. Theoretical formulation

Consider a 2-D homogeneous dielectric cylinder embedded in a half-space material medium as shown in Fig. 1. The cylinder is parallel to z axis buried below a planar interface separating two homogeneous half-spaces: the air (ε_1, μ_1) and the earth (ε_2, μ_2). The cross section of the object is starlike that can be representation in polar coordinates in the x-y plane with respect to the center position (X_O, Y_O). The permittivity and permeability of the buried dielectric object are denoted by (ε_3, μ_3), respectively. The dielectric object is illuminated by Gaussian pulse line source located at the points denote by Tx in the first layer and scattered waves are recorded at those points denoted by Rx in the same layer. The computational domain is discretized by Yee cells. It should be mentioned that the computational domain is surrounded by the optimized PML absorber [22] to reduce the reflection from the environment-PML interface.

2.1. Forward problem

The direct scattering problem is to calculate the scattered electric fields while the shape, location and permittivity of the scatterer are given. The shape function $F(\theta)$ of the scatterer is described by the

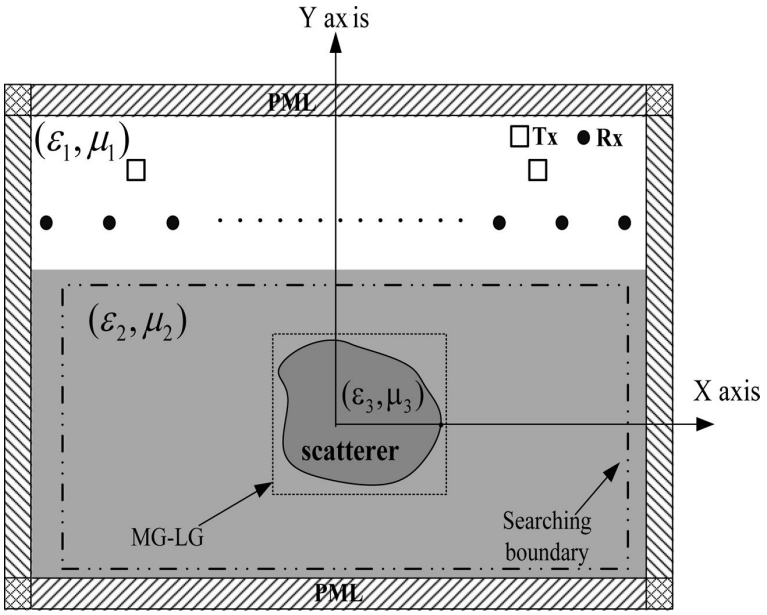

Fig. 1. Geometry for the inverse scattering of a dielectric cylinder of arbitrary shape in free space.

trigonometric series in the direct scattering problem.

$$F(\theta) = \sum_{n=0}^{N/2} B_n \cos(n\theta) + \sum_{n=1}^{N/2} C_n \sin(n\theta) \tag{1}$$

In order to closely describe the shape of the cylinder for both the forward and inverse scattering procedure, the subgridding technique is implemented in the FDTD code, the details are presented next.

2.2. Subgrid FDTD

A major problem in EM modeling by FDTD method is about local fine structures. These structures require a finer cell size than elsewhere and overload the computational cost. The subgridding scheme is proposed to overcome the above drawback in FDTD. A subgridding scheme is employed to divide the problem space into regions with different grid sizes. The grid size in coarse region is about $(\frac{1}{20} \sim \frac{1}{10}\lambda_{\max})$ as in normal FDTD, while in the fine region the grid size is scaled by an integer ratio. As an example, the Yee cells with subgridding structure are shown in Fig. 2, of which the scaling ratio is 1:3. The capital and small case letters stand for EM fields on the major grids and local grids, respectively. If the scaling ratio is set at odd-ratio, then the fields are collocated in space at coarse and fine region. The e fields inside the fine region can be updated through the normal Yee-cell algorithm except those at the MG-LG boundary. The noncollocated magnetic field at the MG-LG interface can be obtained by linearly interpolation. The time interpolation of the fine grid magnetic field at the MG-LG interface is performed using the parabolic interpolation calculation. The above is only a brief introduction to the subgriding FDTD. More details on subgriding FDTD can be found in [20]. The flow chart associated with subgrid FDTD computing procedure is shown in Fig. 3.

For the time domain scattering and/or inverse scattering problem, the scatterers can be assigned with the fine region such that the fine structure can be easily described. If higher resolution is needed, only

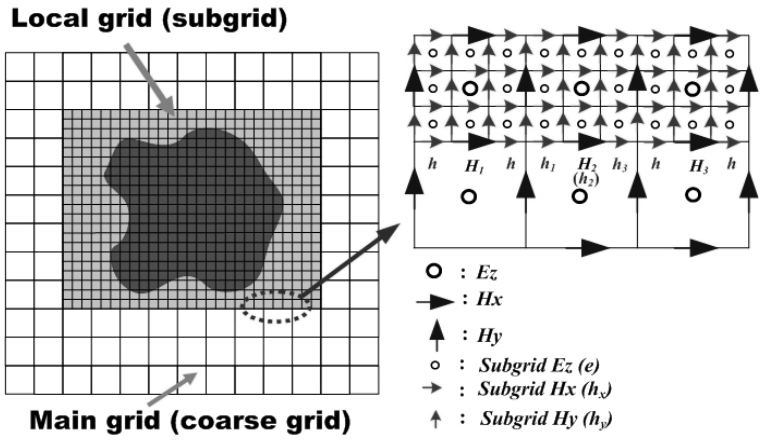

Fig. 2. The structure of the TM_z FDTD major grids and local grids for the scaling ratio (1:3), H fields are aligned with the MG-LG boundary.

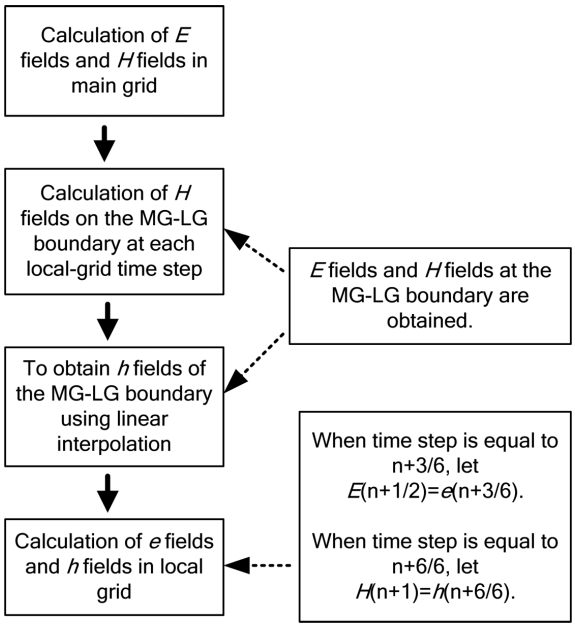

Fig. 3. The flowchart to update the (E, H) fields on the major grids and (e, h) fields on local grids.

the fine region needs to be rescaled using a higher ratio for subgridding. This can avoid gridding the whole problem space using the finest resolution such that the computational resources are utilized in a more efficient way, which is quite important for the computational intensive inverse scattering problems.

2.3. Inverse problem

For the inverse scattering problem, the shape, location and permittivity of the dielectric cylinder are reconstructed through the given scattered electric fields obtained at the receivers. This problem is formulated into an optimization approach, for which the global searching scheme DDE is employed to

minimize the following objective function (*OF*):

$$OF = \frac{\sum_{n=1}^{N_i}\sum_{m=1}^{M}\sum_{k=0}^{K}\left|E_z^{\exp}(n,m,k\Delta t) - E_z^{cal}(n,m,k\Delta t)\right|}{\sum_{n=1}^{N_i}\sum_{m=1}^{M}\sum_{k=0}^{K}\left|E_z^{\exp}(n,m,k\Delta t)\right|} \tag{2}$$

where $E_z^{\exp}$ and E_z^{cal} are the experimental electric fields and calculated electric fields, respectively. The N_i and M are the total number of the transmitters and receivers, respectively. K is the total time step number of the recorded electric fields.

2.4. Dynamic Differential Evolution (*DDE*)

Differential evolution (DE) is a population-based, self-adaptive and parallel direct search optimization method that is proposed by Storn and Prince in 1995 [23]. DE starts with an initial population of potential solutions that is composed by a group of randomly generated individuals which represents the dielectric constant, center position and the geometrical radiuses of the cylinders. Each individual in DE is a D-dimensional vector consisting of D optimization parameters. The initial population may be expressed by $\{x_i\colon i = 1, 2, \cdots, Np\}$, where *Np* is the population size. After initialization, DE performs the genetic evolution until the termination criterion is met. DE, like other EAs, also relies on the genetic operations (mutation, crossover and selection) to evolve generation by generation. In general, a typical DE optimizer goes through the following six procedures:

1. Initialize a starting population: DE is initialized with a population that is composed by a group of randomly generated candidate individuals. Individuals in DE represent a set of D-dimensional vectors in the parameter space for the problem, $\{x_i : i = 1, 2, \cdots, Np\}$, where D is the number of parameters to be optimized and *Np* is the population size.
2. Evaluate the population using objective function: After initialization, DE evaluates the objective function Eq. (2) for each individual in the population.
3. Perform mutation operation to generate trial vectors: The mutation operation of DE is performed by arithmetical combination of individual. For each parameter vector x_i of the parent generation, a trial vector v_i is generated according to following equation:
$$v_i^g = x_{best}^g + \varphi \cdot (x_{r1}^g - x_{r2}^g), \quad i \neq r_1 \neq r_2 \tag{3}$$
where $\varphi > 0$, is weighting factor that control the amplification of the differential variation ($x_{r1}^g - x_{r2}^g$). The indices i, r_1 and r_2 of individuals are randomly chosen. The subscript g stands for the generation index of the parent generation. The *best* refer to the optimal individual in the parent population.
4. Perform crossover operation with probability of crossover *CR* to deliver crossover vectors: The crossover operation in DE is performed to increase the diversity of the parameter vectors. This operation is similar to the crossover process in GAs. However, The crossover operation in DE just allows to deliver the crossover vector u_i by mixing component of the current vector x_i and the trial vector v_i. It can be expressed as:
$$u_i^g(j) = \begin{cases} v_i^g(j), & if \;\; Rand(j) < CR \\ x_i^g(j), & otherwise \end{cases} \tag{4}$$
where CR is the probability of crossover, $CR \in$ (0,1). $Rand(j)$ is the random number generated uniformly between 0 and 1.

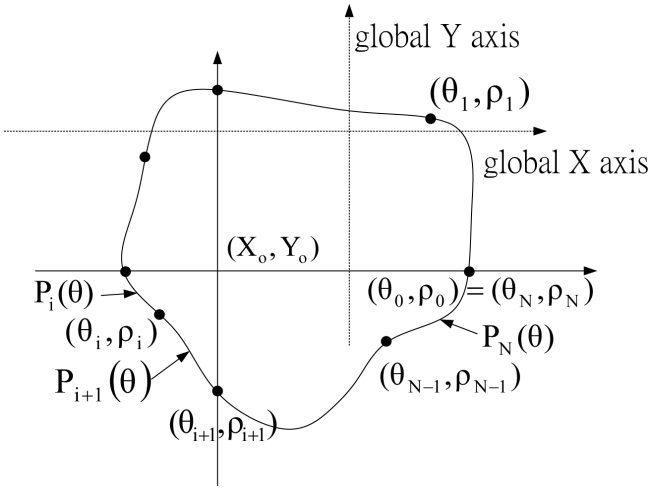

Fig. 4. A cylinder of arbitrary shape is described in terms of a closed cubic spline.

5. Perform selection operation to produce offspring: Selection operation is conducted by comparing the parent vector x_i^g with the crossover vectors u_i^g. The vector with smaller objective function value is selected as a member of the next generation. Explicitly, the selection operation for the minimization problem is given by:

$$x_i^{g+1} = \begin{cases} u_i^g, & if \;\; OF(u_i^g) < OF(x_i^g) \\ x_i^g, & otherwise \end{cases} \tag{5}$$

6. Stop the process and print the best individual if the termination criterion is satisfied, else go to step II.

A modified DE namely dynamic differential evolution, DDE, is proposed to speedup the convergence of the DE [19]. The key distinction between a DDE and a typical DE is on the population updating mechanism. In a typical DE, all the update actions of the population are performed at the end of the generation of which the implementation is referred to as static updating mechanism. Alternatively, the updating mechanism of DDE is carried out in a dynamic way: each parent individual would be replaced by her offspring if the offspring has obtained a better objective function value than its parent. Thus, DDE can respond the progress of population status immediately and yield faster convergence speed than the typical DE. Based on the convergent characteristic of DDE, we are able to reduce the numbers of objective function evaluation and reconstruct the microwave image efficiently.

2.5. Cubic spline interpolation technique

In order to reduce the unknowns required to describe a cylinder of arbitrary cross section, the shape function of the cylinder is expressed in terms of a cubic spline. As shown in Fig. 4, the cubic spline consists of the polynomials of degree 3 $P_i(\theta)$, $i = 1,2, \cdots, N$, which satisfy the following smooth conditions:

$$P_i(\theta_i) = P_{i+1}(\theta_i) \equiv \rho_i$$

$$P_i'(\theta_i) = P_{i+1}'(\theta_i) \quad i = 1, 2, \cdots, N \tag{6}$$

$$P_i''(\theta_i) = P_{i+1}''(\theta_i)$$

and

$$\begin{aligned} P_1(\theta_0) &= P_N(\theta_N) \\ P_1'(\theta_0) &= P_N'(\theta_N) \equiv \rho_N' \\ P_N''(\theta_i) &= P_N''(\theta_N) \end{aligned} \tag{7}$$

Through the interpolation of the cubic spline, an arbitrary smooth cylinder can be easily described through the radius parameters $\rho_1, \rho_2, \cdots, \rho_N$ and the slope ρ_N', of which the details are referred to [21].

It should be noted that the dielectric constant and center position of the cylinder plus the radiuses of the geometrical spline used to describe the shape of the cylinder will be determined by the DDE optimization scheme.

3. Numerical results

As shown in Fig. 1, the problem space is divided in 128 $\times$ 68 grids with the grid size $\Delta x = \Delta y =$ 5.95mm. The homogeneous dielectric cylinder is buried in lossless half space ($\sigma_1 = \sigma_2 = 0$). The transmitters and receivers are placed in free space above the homogeneous dielectric. The permittivities in region 1 and region 2 are characterized by $\varepsilon_1 = \varepsilon_0$ and $\varepsilon_2 = 2.3\varepsilon_0$, respectively, while the permeability μ_0 is used for each region, i.e., only non-magnetic media are concerned here. The distance between half-space interface and the original cylinder is 89.2mm. The cylindrical object is illuminated by a transmitter at two different positions, $N_i = 2$, which are located at ($-$143mm, 178.5mm) and (143mm, 178.5mm), respectively. The scattered E fields for each illumination are collected at fifteen receivers, $M = 15$, which are equally separated by 47.8mm along the line of distance 48mm from the half-space interface. The excitation waveform $I_z(t)$ of the transmitter is the Gaussian pulse, given by:

$$I_z(t) = \begin{cases} Ae^{-\alpha(t-\beta\Delta t)^2}, & t \leqslant T_w \\ 0, & t > T_w \end{cases} \tag{8}$$

where $\beta = 32$, $A = 1000$, $\Delta t = 13.337\ ps$, $T_w = 2\beta\Delta t$, and $\alpha = \left(\frac{1}{4\beta\Delta t}\right)^2$.

The time duration is set to 300 $\Delta t (K = 300)$. Note that in order to describe the shape of the cylinder more accurately, the subgridding FDTD technique is employed both in the forward scattering (1:9) and the inverse scattering (1:5) parts – but with different scaling ratios as indicated in the parentheses. For the forward scattering, the E fields generated by the FDTD with finer subgrids are used to mimic the experimental data in Eq. (2). The reconstruction ideas are carried out through a home-made Fortran program that runs on an Intel PC (2.83 GHz/ 2G memory/500 G).

Four examples are investigated for the inverse scattering of the proposed structure by using the DDE scheme. There are twelve unknown parameters to retrieve, which include the center position (X_O, Y_O), the radius ρ_i, $i = 1, 2, \cdots, 8$ of the shape function and the slope ρ_N' plus the relative permittivity of the object, $\varepsilon_r = \varepsilon_3/\varepsilon_0$. Very wide searching ranges are set for the DDE to optimize the objective function given by Eq. (2). The parameters and the corresponding searching ranges are listed as follows: $-$208.3mm $\leqslant X_O \leqslant$ 208.3mm, $-$137.8mm $\leqslant Y_O \leqslant$ 77.4mm, 0mm $\leqslant \rho_i \leqslant$ 71.4mm, i = 1,2, $\cdots$,

Table 1
The errors of the reconstructed shape function and the dielectric constant by using different subgridding ratios

Subgridding ratio	DF	DIPE
1:1	8.25%	1.16%
1:3	5.85%	0.16%
1:5	1.9%	0.15%
1:7	0.89%	0.14%

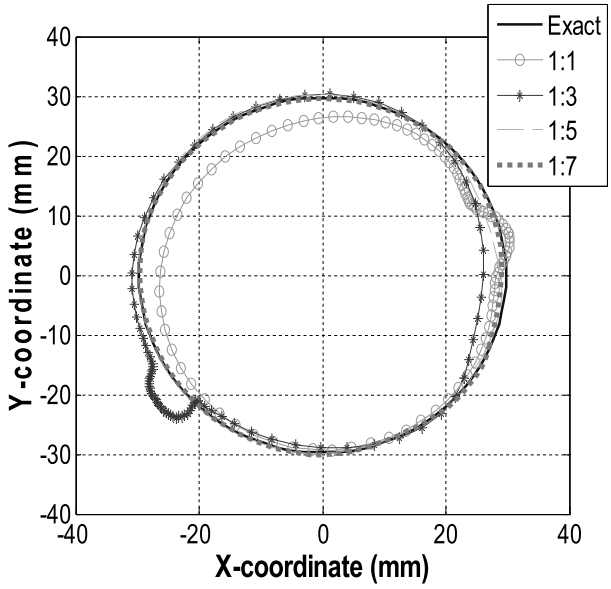

Fig. 5. The reconstructed shapes of the cylinder for example 1 by using different scaling ratios for the subgrid.

8, $-1 \leqslant \rho'_N \leqslant 1$ and $1 \leqslant \varepsilon_r \leqslant 16$. The operational coefficients for the DDE are set as below: The crossover rate $CR = 0.8$. The weighting factor $\varphi = 0.8$ and the population size $Np = 120$.

The key distinction between standard uniform grid FDTD and sub-grid FDTD is on the convergence and the computation time. As the complicated geometry features with high dielectric material are confined to a small region of the coarse main grid; application of sub-grid technique can result in large savings of computer time and memory for the FDTD method. Thus, in this study, sub-grid FDTD technique is implemented to efficiently describe the details of the dielectric cylinders shape. For the first example, the dielectric cylinder with shape function $F(\theta) = 29.75$ (unit: mm) and relative permittivity $\varepsilon_r = 3$ is tested. In Fig. 5, the standard FDTD with uniform grid of (1:1) case is compared with the sub-grid FDTD cases of different scaling ratios (1:3), (1:5) and (1:7), respectively. The reconstructed details are listed in Table 1. Obviously, the results obtained by using the standard FDTD with uniform grid (1:1) are not as good as those of the sub-grid FDTD cases. It also suggests that the scaling ratio (1:5) is suitable for the following examples to be studied. On the other hand, in order to achieve the same accuracy for the standard FDTD with uniform grid, the gird size of the whole space has to be reduced to smoothly describe the geometry of the dielectric cylinder, however, the cost of the computation time would be increased quite a lot, 4.17 times as compared to the subgrid FDTD scheme of (1:5) case, for example.

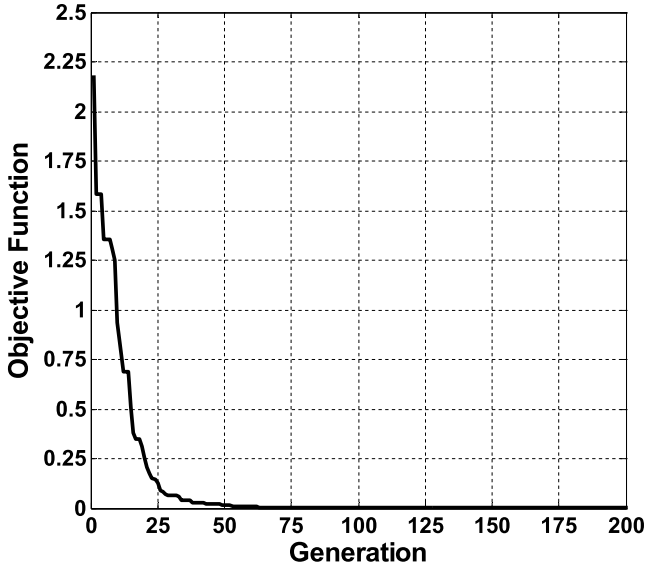

Fig. 6. The average fitness value versus generation for example 2 using the Gaussian pulse illumination as the DDE executed seven times out of ten.

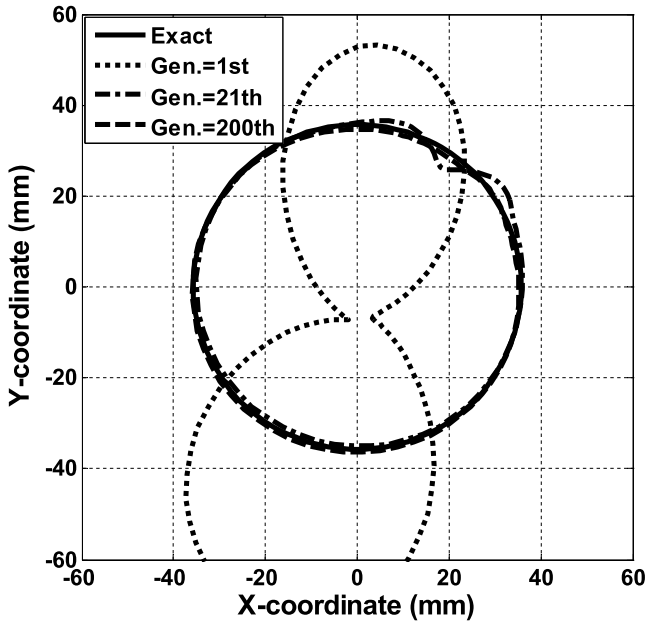

Fig. 7. The reconstructed shape of the cylinder at different generations for example 2.

For the second example, the dielectric cylinder with shape function $F(\theta) = 35.7$ (unit: mm) and relative permittivity $\varepsilon_r = 3.7$ is considered. The average convergence curve of objective function versus generation as the DDE executed seven times is shown in Fig. 6. The reconstructed shape function is the best individual of the population is plotted in Fig. 7 for different generations. The r.m.s. error (DF) of the reconstructed shape $F^{cal}(\theta)$ and the relative error (DIPE) of ε_r^{cal} with respect to the exact values versus

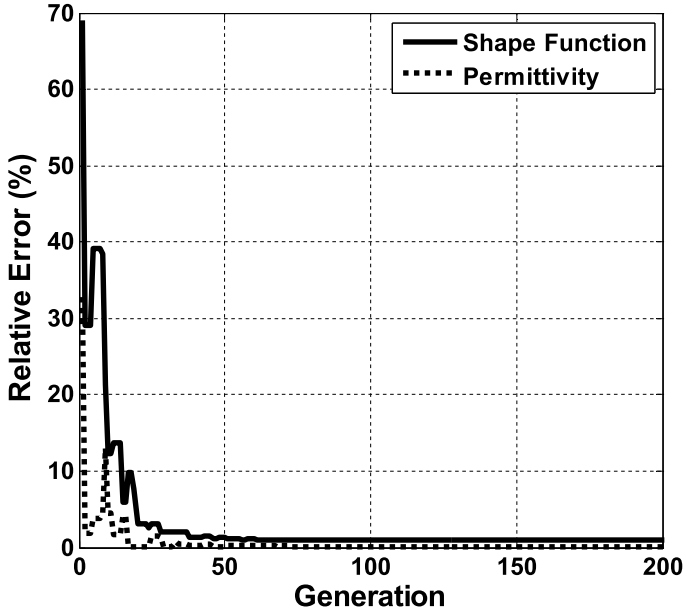

Fig. 8. Shape error and permittivity error versus generation for example 2.

generation are shown in Fig. 8. It is shown that the DDE scheme is able to achieve good convergences within 50 generations. Here, DF and DIPE are defined as

$$DF = \{\frac{1}{N'}\sum_{i=1}^{N'}[F^{cal}(\theta_i) - F(\theta_i)]^2/F^2(\theta_i)\}^{1/2} \tag{9}$$

$$DIPE = \frac{\left|\varepsilon_r^{cal} - \varepsilon_r\right|}{\varepsilon_r} \tag{10}$$

where the N' is set to 720. The r.m.s. error DF is about 0.97% and DIPE $=$ 0.14% in final generation.

The reconstructed images for different generations and the relative error of the third example are shown in Figs 9 and 10, respectively. The shape function of this object is given by $F(\theta) = 23.88 + 11.9\cos(\theta) - 5.95\sin(2\theta)$mm and the relative permittivity of the object is $\varepsilon_r = 2.8$. Figure 10 shows that the relative errors of the shape and the permittivity decrease quickly and good convergences are achieved within 30 generations. The r.m.s. error DF is about 2.8% and DIPE $=$ 0.42% in final generation. From the reconstructed results these two objects, we conclude the DDE scheme can be used to reconstruct buried dielectric cylinder successfully even initial guess is far away from exact one.

In the fourth example, let us consider the problem for dielectric cylinders with high permittivity. The shape function of this object is given by $F(\theta) = 29.7 + 5.95\cos(3\theta)$mm and the relative permittivity of the object is $\varepsilon_r = 8.2$. The reconstructed images at different generations and the relative error of the final example are shown in Figs 11 and 12, respectively. As shown in Fig. 12, the r.m.s. error DF is about 1.7% and DIPE $=$ 0.67% in final generation. From the reconstructed results of this example, we conclude the proposed method is able to reconstruct buried dielectric cylinder successfully when the dielectric object with high-contrast permittivity. In order to investigate the sensitivity of the imaging algorithm against random noise, the additive white Gaussian noise of zero mean is added into the experimental electric

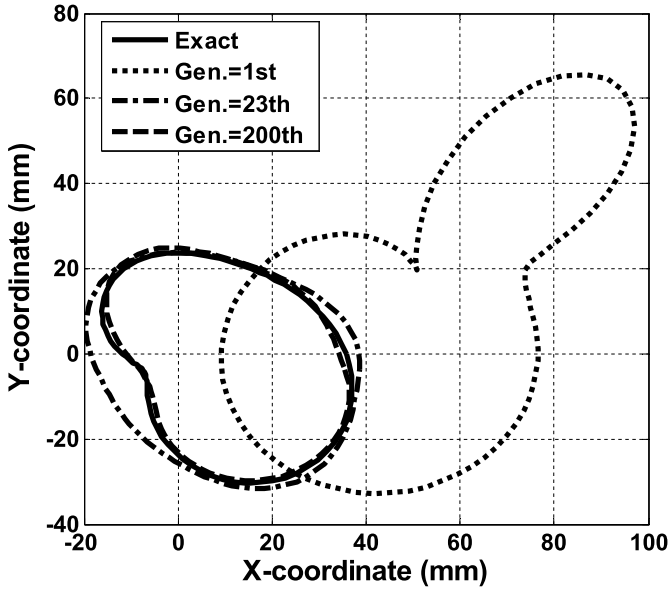

Fig. 9. The reconstructed cross section of the cylinder of example 3 at different generations.

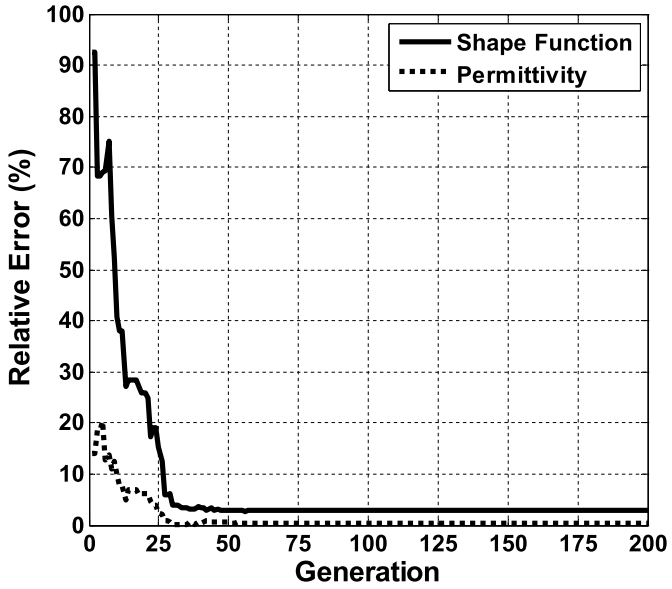

Fig. 10. Shape-function error and permittivity error versus generations for example 3.

fields. Normalize standard deviations of 10^{-4}, 10^{-3}, 10^{-2}, 10^{-1}, 0.2 and 0.5 are used in simulation purpose. The normalized standard deviation is defined as the standard deviation of the Gaussian noise divided by the r.m.s. value of the scattered fields. Figure 13 shows the reconstructed results under the condition that the experimental scattered field is contaminated by noise. It could be observed that good reconstruction has been obtained for both the relative permittivity and shape of the dielectric cylinder when the relative noise level is below 10^{-1}.

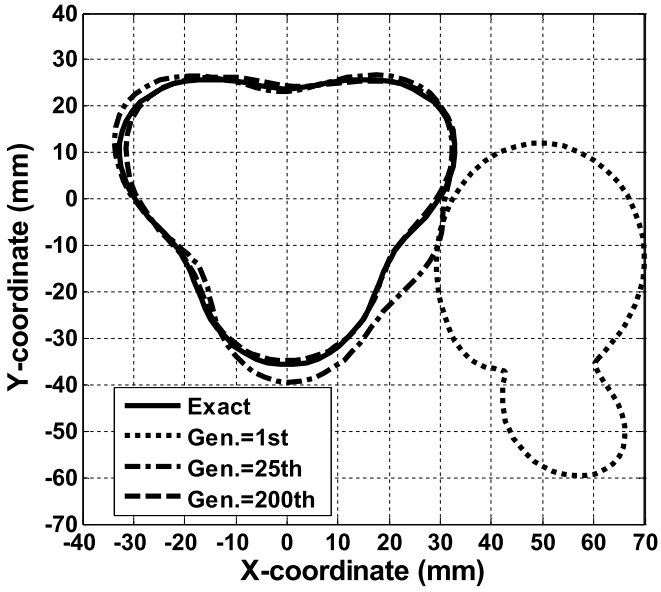

Fig. 11. The reconstructed cross section of the cylinder of example 4 at different generations.

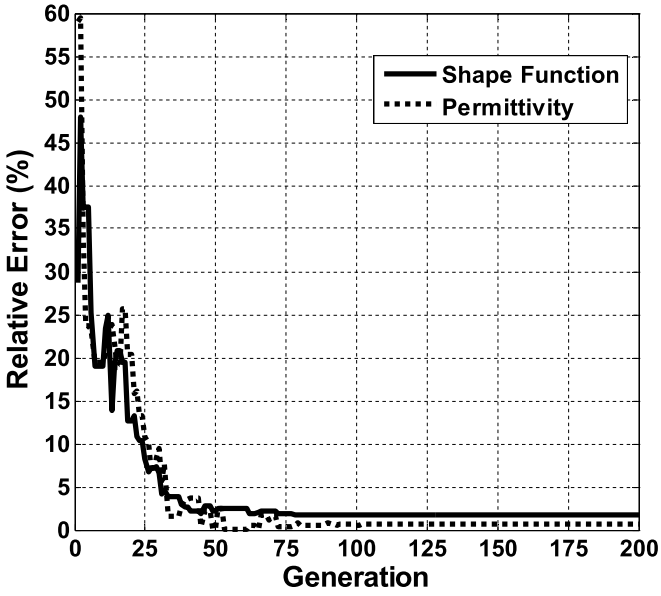

Fig. 12. Shape-function error and permittivity error versus generations for example 4.

4. Conclusion

We present a study of the time domain inverse scattering of homogeneous dielectric cylinders of arbitrary cross section in half space. By combining the FDTD method and the DDE scheme, good reconstructed results are obtained. The subgridding scheme is employed to closely describe the shape of the cylinder for the FDTD method. The forward problem is solved by using the subgridding FDTD

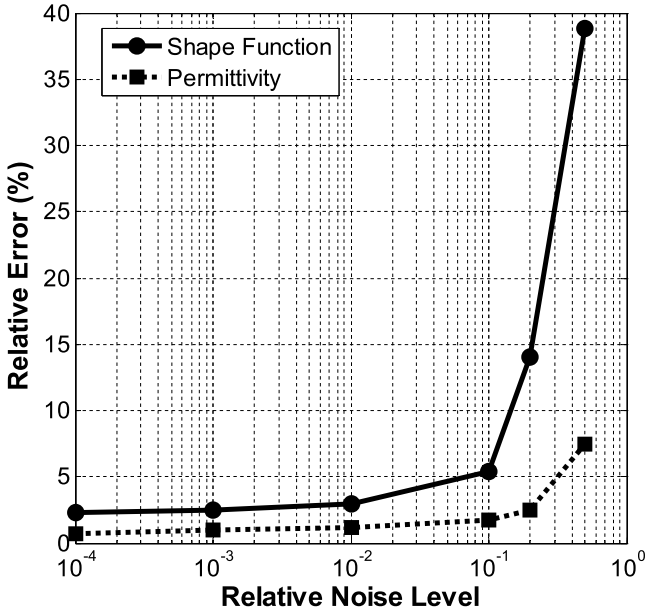

Fig. 13. Shape error and relative permittivity errors as functions of SNR (dB).

method and the shape function of the cylinder is expressed in terms of Fourier series expansion. The inverse problem is reformulated into an optimization one, and then the global searching scheme DDE is employed to search the parameter space. Interpolation technique through cubic spline is utilized to reduce the number of parameters needed to describe an arbitrary shape for the inverse scattering problem. Through the DDE scheme, the shape, location and dielectric constant of the object can be successfully reconstructed even when the dielectric constant is fairly large. This study shows that even when the initial guess is far from the exact one, the DDE can still yield a good solution for the properties of the object, while the gradient-based methods often get stuck in local extremes. The effects of noise upon the microwave imaging are examined, and good reconstruction has been obtained even in the presence of white Gaussian noise in experimental data.

References

[1] D. Colton and R. Kress, *Inverse Acoustic and Electromagnetic Scattering Theory*, Springer-Verlag, New York, 1992.
[2] A. Kirsch and R. Kress, Uniqueness in inverse obstacle scattering, *Inverse Problems* **9** (1993), 285–299.
[3] A. Yapar, H. Şahintürk, I. Akduman, and R. Kress, One-dimensional profile inversion of a cylindrical layer with inhomogeneous impedance boundary: a Newton-type iterative solution, *IEEE Transactions on Geoscience and Remote Sensing* **43**(10) (October 2005), 2192–2199.
[4] C.C. Chiu and Y.W. Kiang, Microwave imaging of multiple conducting cylinders, *IEEE Transactions on Antennas and Propagation* **40**(8) (August 1992), 933–941.
[5] S. Caorsi, A. Massa and M. Pastorino, A computational technique based on a real-coded genetic algorithm for microwave imaging purposes, *IEEE Transactions on Geoscience and Remote Sensing* **38**(4) (July 2000), 1697–1708.
[6] C.H. Sun, C.L. Liu, K.C. Chen, C.C. Chiu, C.L. Li and C.C. Tasi, Electromagnetic Transverse Electric Wave Inverse Scattering of a Partially Immersed Conductor by Steady-State Genetic Algorithm, *Electromagnetics* **28**(6) (Aug. 2008), 389–400.
[7] A. Qing, Electromagnetic inverse scattering of multiple two-dimensional perfectly conducting objects by the differential evolution strategy, *IEEE Transactions on Antennas and Propagation* **51**(6) (2003), 1251–1262.

[8] K.A. Michalski, Electromagnetic imaging of circular-cylindrical conductors and tunnels using a differential evolution algorithm, *Microwave and Optical Technology Letters* **27**(5) (Dec. 2000), 330–334.
[9] I.T. Rekanos and A. Trochidis, Shape reconstruction of two-dimensional acoustic obstacle using particle swarm optimization, *Acta Acustica united with Acustica* **93**(6) (Nov.–Dec. 2007), 917–923.
[10] M. Donelli and A. Massa, Computational approach based on a particle swarm optimizer for microwave imaging of two-dimensional dielectric scatterers, *IEEE Transactions on Microwave Theory and Techniques* **53**(5) (May. 2005), 1761–1776.
[11] W. Yu, Z. Peng and L. Jen, The time-domain Born iterative method for two-dimensional inhomogeneous lossy dielectric, *Journal of Microwaves* **11**(12) (1995).
[12] W.H. Weedon, *Broadband microwave inverse scattering: Theory and experiment*, Ph.D. dissertation, University of Illinois at Urbana-Champaign, 1994.
[13] I.T. Rekanos, Time-domain inverse scattering using lagrange multipliers: an iterative FDTD-based optimization technique, *Journal of Electromagnetic Waves and Applications* **17**(2) (2003), 271–289.
[14] T. Takenaka, H. Jia and T. Tanaka, Microwave imaging of electrical property distributions by a forward-backward time-stepping method, *Journal of Electromagnetic Waves Application* **14** (2000), 1609–1625.
[15] S. He, P. Fuks and G. W. Larson, An Optimization Approach to Time-Domain Electromagnetic Inverse Problem for a Stratified Dispersive and Dissipative Slab, *IEEE Transactions on Antennas and Propagation* **44**(9) (Sept. 1996), 1277–1282.
[16] C.H. Huang, C.C. Chiu, C.L. Li and Y.H. Li, Image Reconstruction of the Buried Metallic Cylinder Using FDTD Method and SSGA, *Progress In Electromagnetics Research* **PIER 85** (2008), 195–210.
[17] C.H. Huang, C.C. Chiu, C.L. Li and K.C. Chen, Time Domain Inverse Scattering of a Two-Dimensional Homogenous Dielectric Object with Arbitrary Shape by Particle Swarm Optimization, *Progress In Electromagnetic Research* **PIER 82** (2008), 381–400.
[18] X.L. Travassos, D.A.G. Vieira, N. Ida, C. Vollaire and A. Nicolas, Inverse Algorithms for the GPR Assessment of Concrete Structures, *IEEE Transactions on Magnetics* **44**(6) (June 2008).
[19] A. Qing, Dynamic differential evolution strategy and applications in electromagnetic inverse scattering problems, *IEEE Transactions on Geoscience and Remote Sensing* **44**(1) (2006), 116–125.
[20] M.W. Chevalier, R.J. Luebbers and V.P. Cable, FDTD local grid with materical traverse, *IEEE Trans. Antennas and Propagation* **45**(3) (March 1997).
[21] C. de Boor, *A Practical Guide to Splines*, Springer-Verlag, New York, 1978.
[22] C.L. Li, C.W. Liu and S.H. Chen, Optimization of a PML absorber's conductivity profile using FDTD, *Microwave and Optical Technology Letters* **37**(5) (Jun. 2003), 69–73.
[23] R. Storn and K. Price, Differential Evolution – a Simple and Efficient Adaptive Scheme for Global Optimization over Continuous Spaces, Technical Report TR-95-012, International Computer Science Institute, Berkeley, 1995.